RSC Advances

PAPER

View Article Online
View Journal | View Issue

Cite this: *RSC Adv.*, 2017, 7, 32264

Electrocatalytic activity of porous Ni–Fe–Mo–C–LaNi$_5$ sintered electrodes for hydrogen evolution reaction in alkaline solution

Liang Wu,[abc] Xiaohua Guo,[abc] Yang Xu,[abc] Yifeng Xiao,*[abc] Jinwen Qian,[abc] Yanfei Xu,[abc] Zhuo Guan,[abc] Yuehui He[d] and Yi Zeng[d]

Received 13th January 2017
Accepted 14th May 2017

DOI: 10.1039/c7ra00550d

rsc.li/rsc-advances

The hydrogen evolution reaction (HER) was studied in 6 M KOH solution at temperatures ranging between 303 K and 353 K on a porous Ni–Fe–Mo–C–LaNi$_5$ electrode. By using steady-state polarization curves and electrochemical impedance spectroscopy (EIS), the surface roughness factor and the intrinsic activities of the porous Ni–Fe–Mo–C–LaNi$_5$ electrode have been determined. The Tafel slope of the best-performing porous Ni–Fe–Mo–C–LaNi$_5$ cathode materials is 140 mV dec^{-1}, and the exchange current density is 9.9×10^{-4} A cm^{-2} at elevated temperature. The roughness factor is 8600, which was obtained for the HER on studied electrodes in 6 M KOH solution at 323 K temperature using the EIS data and complex nonlinear least square (CNLS) approximation method. These techniques also permitted us to determine the mechanism and kinetics of the HER on the investigated electrode. The overall experimental data indicates that the porous Ni–Fe–Mo–C–LaNi$_5$ electrode yields electrocatalytic activity in the HER. Nevertheless, when the effect of the surface roughness is taken into consideration, it is demonstrated that alloying Ni with Fe, Mo, C and LaNi$_5$ results in an increased electrocatalytic activity in the HER when comparing to pure Ni. This is due to an improved intrinsic activity of the material, which is explained on the basis of the synergism among the catalytic properties of Ni and of Fe, Mo, and induced by C embedded into Ni–Fe matrix and Ni–Fe–Mo matrix. LaNi$_5$ enhances the H adsorption on the electrode surface and mainly plays a role of hydrogen storage for HER.

1. Introduction

Hydrogen, as a clean and sustainable chemical fuel, is recognized as the most promising substitute for fossil fuels in the future energy infrastructure.[1–3] Water electrolysis is a renewable and secure way to create hydrogen of high purity with zero pollutants emission.[4,5] The hydrogen evolution reaction (HER) is one of the most frequently studied electrochemical reactions for different reasons. First, the reaction takes place through a limited number of reaction steps with only one reaction intermediate involved.[6–10] Second, it has an industrial/technological interest in the alkaline water electrolysis.[11–13] Currently, the state-of-art cathode materials for the HER are based on Pt and Pt-based materials,[14,15] but their broad applications are restricted by the high cost and resource scarcity. Thus, it is a crucial task to develop effective earth-abundant HER electrocatalysts to replace the precious metals. Among the non-noble metals, Ni and Ni-based electrode materials have been widely considered as promising electrocatalytic materials due to their comparatively large electrocatalytic activity and good stability for HER in alkaline solutions.[16] Two main approaches including alloying Ni with some other metals or non-metals[17–24] and compositing Ni with active nano-sized particles[25–30] have been taken to enhance the intrinsic activity and/or increase the real surface area of electrode materials for HER.

In general, the development of novel materials with low overpotential towards the HER could be based on two basic characteristics, namely, increase of intrinsic catalytic activity by use of multicomponent catalysts and increase of the real surface area. Ni-based alloys have represented high catalytic activity in HER and exhibited better catalytic capability than single Ni catalyst for synergistic electronic effect among alloys.[31,32] In previous studies, a series of ternary Ni composites such as Ni–Mo–Fe, Ni–Mo–Cu, Ni–Mo–Zn, Ni–Mo–W, Ni–Mo–Co and Ni–Mo–Cr were studied for hydrogen evolution and the authors reported that the best and most stable cathode was Ni–Mo–Fe.[33–35] High stability of amorphous Ni–Mo–Fe electrode was confirmed by other authors who tested the electrode with

---

[a] School of Mechanical Engineering, Xiangtan University, Hunan 411105, China. E-mail: sanyxyf@163.com

[b] Key Laboratory of Welding Robot and Application Technology of Hunan Province, Xiangtan University, Xiangtan 411105, China

[c] Engineering Research Center of Complex Tracks Processing Technology and Equipment of Ministry of Education, Xiangtan University, Xiangtan 411105, China

[d] State Key Laboratory of Powder Metallurgy, Central South University, Changsha 410083, China

current interruptions.[36] Besides, many interests have been devoted to the study of multicomponent alloy electrodes. It was found that Ni–Fe–C cathodes prepared by electrodeposition had high catalytic activity and stability for the HER in sodium hydroxide solution, in which the observed activity was mainly due to the intrinsic activity induced by carbon embedded into Ni–Fe matrix.[37–39] Moreover, Machida and Enyo[40] published that $LaNi_5$ and other combinations of rare-earth metals and Ni, used as cathode come close to the reversible hydrogen electrode over a wide range of current densities. The authors highlighted the good performance of the electrode materials and proposed that the HER on the $LaNi_5$ alloys proceeds *via* the Volmer–Tafel reaction route with mixed rate determining characteristics. Based on the above results, it is possible to produce new kinds of porous alloys which combine both a high surface area and good intrinsic catalytic activity in the process of the HER.

The present study was undertaken in order to investigate the electrochemical properties of Ni–Fe–Mo electrode materials, by adding carbon content and rare earths (RE) powders using solid state reaction and comparing with traditional electrocatalytic nickel activity on HER. The aim of the present work is to study the electrocatalytic performance of the developed electrodes for HER, distinguishing the effect of both the surface roughness and the intrinsic activity of the material, by the determination of the real active surface area of the catalyst, in terms of R_f. The mechanisms and kinetics of the HER on these electrodes have also been determined.

2. Experimental

2.1. Preparation of porous Ni–Fe–Mo–C–$LaNi_5$ electrode

Pure commercial powders of Ni (3–5 μm), Fe (3–5 μm), Mo (3–5 μm), C (3–5 μm), $LaNi_5$ (40–70 μm) were mixed in the ratio of 70 : 25 : 3 : 1 : 1 by weight. The powders were ball-milled for 10 h using a mixer, and pressed into compact specimens with dimensions of 28.84 mm × 7.5 mm × 4 mm under a pressure of 50 MPa. The specimens were then sintered in a vacuum furnace under 1×10^{-3} Pa at temperatures of 820 °C for a duration of 30 min. Based on our previous work, porous Ni–Cr–Fe with the composition of 7 : 2 : 1 sintered under a temperature of 850 °C displayed the best activity for the HER.[41] Therefore, porous Ni–Fe–Mo–C materials with powder compositions of 70 : 27 : 2 : 1, 70 : 26 : 3 : 1 and porous Ni–Fe–Mo–C–$LaNi_5$ materials with powder compositions of 70 : 26 : 2 : 1 : 1 and 70 : 25 : 3 : 1 : 1 by weight and sintering temperatures of 820 °C, 850 °C and 880 °C were also prepared for comparing the HER activities.

X-ray diffraction (XRD) (Rigaku D/max-2500, graphite monochromator, Cu Kα) and field-emission scanning electron microscopy (SEM) (NOVA NANOSEM 230) were employed to identify the phase composition, crystalline structures and surface morphology of the materials. The open porosity was measured by the Archimedes method in water based on the following principles: the mass (W_S) of a dried porous disc and the mass (W_x) of the porous disc filled with the wax with a density of ρ_x were weighted in air. The external volume (V_x) of the waxed disc could be determined in water according to the Archimedes method. Then, the open porosity (θ_p) could be calculated by the expression: $\theta_p = (W_x - W_S)/(V_x{*}\rho_x)$.[42]

Japanese manufacturing electron microprobe (EPMA, JEOLCO, JXA8230 and JXA-8530-f) was employed to measure the distribution of phase elements.

2.2. Electrochemical measurements

The developed electrodes were characterized by means of steady-state polarization curves and electrochemical impedance spectroscopy (EIS). All these tests were performed in oxygen free 6 M KOH solutions which were achieved by bubbling N_2 for 15 min before the experiments.

Polarization curves were potentiodynamically recorded from −2.0 V *vs.* Hg/HgO up to the equilibrium potential at a scan rate of 1 mV s^{-1}, and at six different temperatures: 303 K, 313 K, 323 K, 333 K, 343 K and 353 K. Before the tests, the working electrode was held at −1.5 V (*vs.* $V_{Hg/HgO}$) in the same solution in order to reduce the oxide film existing on the surface electrode layer, for the time needed to establish reproducible polarization diagrams.

EIS measurements were performed after obtaining the polarization curves. Alternating current impedance measurements were carried out at different cathodic overpotentials, and at the following temperatures: 303 K, 323 K, and 353 K. The measurements were made in the frequency range of 10 kHz to 10 mHz. Ten frequencies per decade were scanned using a sinusoidal signal of 10 mV peak-to-peak. The complex nonlinear least square (CNLS) fitting of the impedance data was carried out with the Zview 2.0 software package.

All the electrochemical tests were carried out using a CS350 electrochemical workstation in a standard three-electrode electrochemical cell in 6 M KOH solution. Pt foil and Hg/HgO electrodes were used as the counter and reference electrodes, respectively. The latter was connected to the working electrode *via* a Luggin capillary positioned close to the working electrode.

3. Results and discussion

3.1. Characterization of porous Ni–Fe–Mo–C–$LaNi_5$ cathode materials

Fig. 1a shows a typical XRD pattern of a prepared porous Ni–Fe–Mo–C–$LaNi_5$ alloy. The pattern indicates that the prepared porous material has a very similar crystal structure to that of Ni owing to the high solubility of Fe, Mo and C in the Ni matrix. The diffraction peaks are (111), (200) and (220). Fig. 1b shows the negative shift of the (111) peak of the porous Ni–Fe–Mo–C–$LaNi_5$ cathode material relative to that of the porous Ni. Compared with Ni, the (111) peak of the Ni–Fe–Mo–C–$LaNi_5$ alloy shows an obvious shift to the left (lower angle) due to the solid solution of Mo, Fe and C in the Ni.

Scanning electron micrographs (SEM) of the porous Ni–Fe–Mo–C–$LaNi_5$ cathode material is shown in Fig. 2. The porous microstructure indicates that the fabricated porous Ni–Fe–Mo–C–$LaNi_5$ electrode has a high open porosity. It is widely accepted that one of the methods for the activity enhancement of cathode materials is the increase of the surface area.

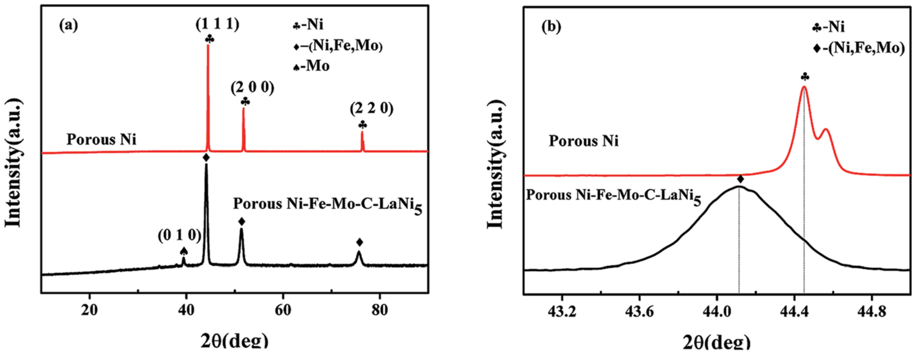

Fig. 1 (a) XRD pattern of the porous Ni–Fe–Mo–C–$LaNi_5$ cathode material and porous Ni; (b) the negative shift of the (111) peak of the porous Ni–Fe–Mo–C–$LaNi_5$ cathode material relative to that of the porous Ni.

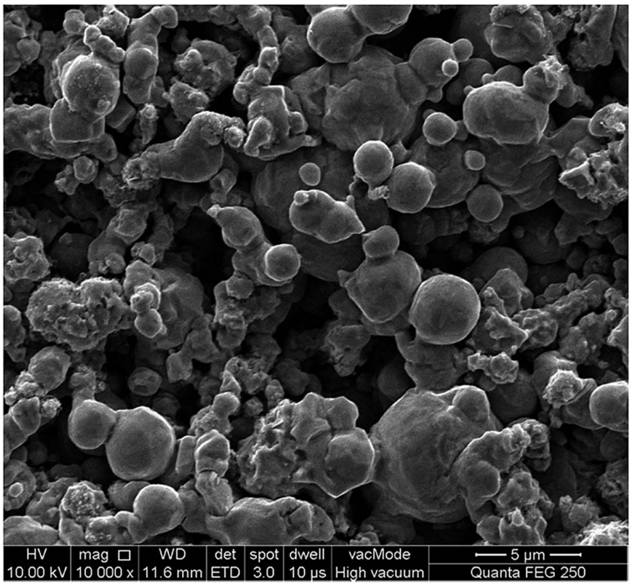

Fig. 2 SEM images of the freshly prepared porous Ni–Fe–Mo–C–$LaNi_5$ electrode.

BSED and EDS maps of porous Ni–Fe–Mo–C–$LaNi_5$ electrode are shown in Fig. 3. There are mainly four parts from the above picture. The main parts of the figure in the dark-grey are Ni–Fe–C solid solution. White parts are mainly Mo particles. Light grey parts are Ni–Fe–Mo–C solid solution. A long strip of material is $LaNi_5$, which does not react with other elements.

EPMA mapping performed on the BSED images (Fig. 4(a)) of the porous Ni–Fe–Mo–C–$LaNi_5$ electrode are shown in Fig. 4. From the Fig. 4(b) and (c), we can see that there are Ni–Fe solid solution generation. Fig. 4(d) shows that Mo elements exist in the form of aggregate. However, there are small number of Ni, Fe elements distributing on Mo particles, forming Ni–Fe–Mo–C solid solution. La elements are mainly enriched in an area, in combination with Fig. 4(e), which are $LaNi_5$ alloy.

EPMA line scanning performed on the BSED images (Fig. 5(a)) of the porous Ni–Fe–Mo–C–$LaNi_5$ electrode is shown in Fig. 5. The left parts of the figure in the dark-grey are Ni, Fe and C elements. The right parts of the figure in the light grey are Ni, Fe, Mo and C elements. And the content of Ni, Fe elements increased gradually in the light grey part. It shows that some Ni, Fe elements diffuse into the Mo particles.

The pore structure parameters of the freshly prepared porous Ni–Fe–Mo–C–$LaNi_5$ cathode material are shown in Table 1. Obviously, the porous Ni–Fe–Mo–C–$LaNi_5$ cathode material has a larger porosity and mean pore size than the porous Ni.

3.2. Polarization measurements

The linear sweep cathodic polarizations of the different kinds of porous Ni–Fe–Mo–C–$LaNi_5$ cathode materials for the HER in 6 M KOH at 303 K are illustrated in Fig. 6. Porous Ni–Fe–Mo–C–$LaNi_5$ materials with the composition of 70 : 25 : 3 : 1 : 1

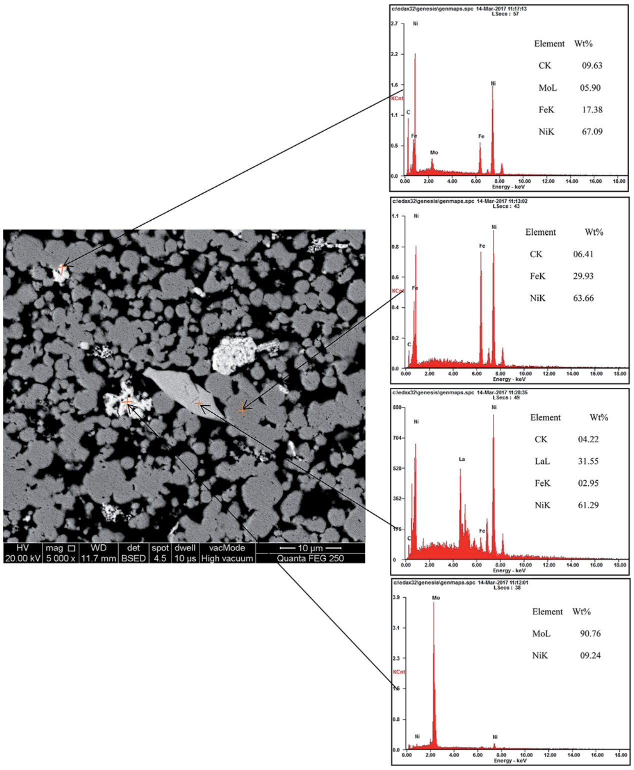

Fig. 3 BSED and EDS of porous Ni–Fe–Mo–C–LaNi5 electrode.

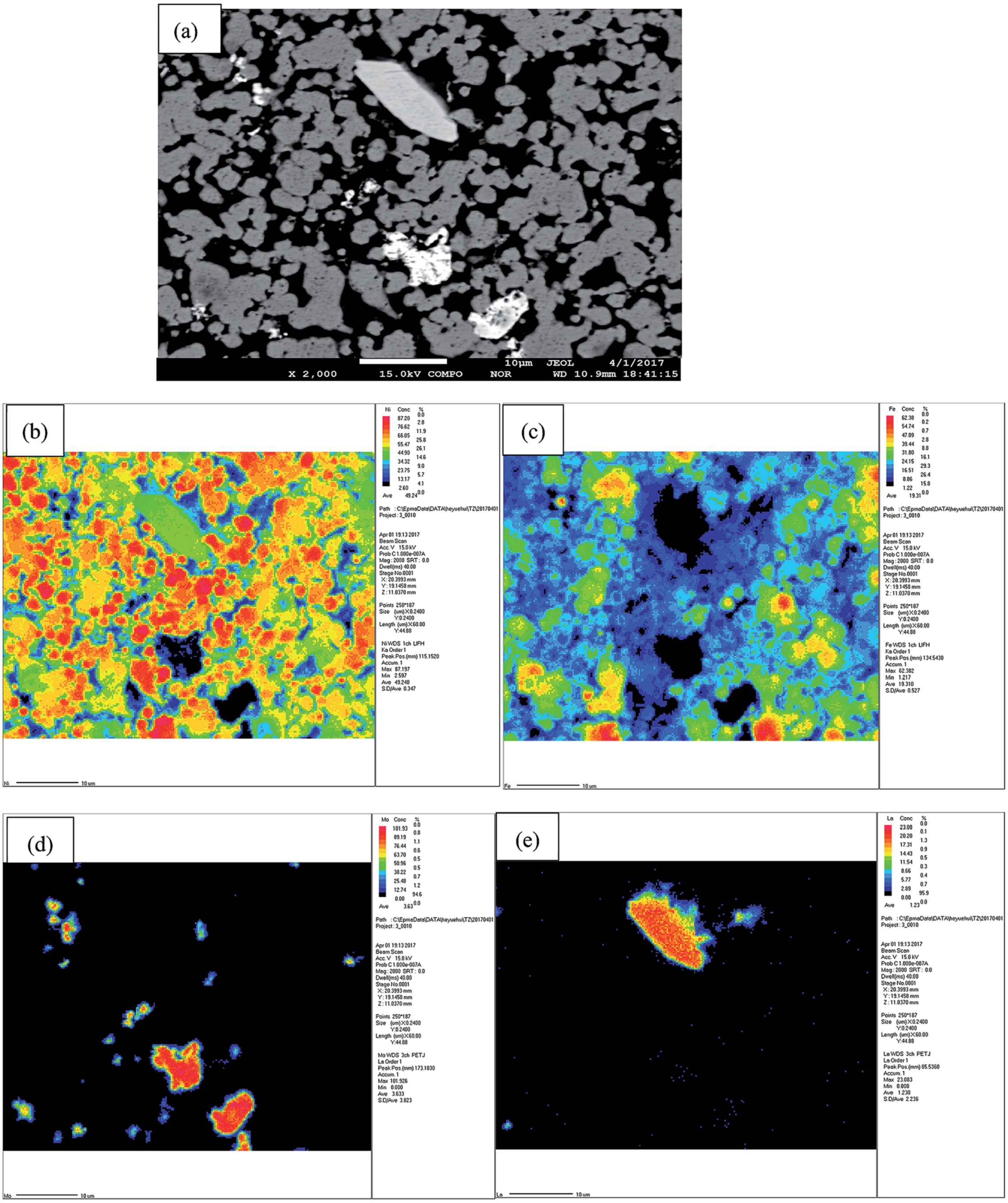

Fig. 4 BSED images (a) and EPMA mappings of porous Ni–Fe–Mo–C–$LaNi_5$ electrode, showing the elemental distribution of Ni (b), Fe (c), Mo (d) and La (e).

sintered at different temperatures all showed excellent activity for the HER, and porous Ni–Fe–Mo–C–$LaNi_5$ with the composition of 70 : 25 : 3 : 1 : 1 sintered under a temperature of 820 °C displayed the best activity for the HER. Without special version, all the figures and tables illustrate the performances of porous Ni–Fe–Mo–C–$LaNi_5$ alloys with the composition of 70 : 25 : 3 : 1 : 1 and under the sintering temperature of 820 °C.

In order to investigate the catalytic activity of the prepared electrocatalysts, Tafel linear polarization measurements were preformed in 6 M KOH solution, and the corresponding electrochemical parameters (Tafel slope, exchange current density, transfer coefficient) were derived from the recorded curves. Fig. 7 shows a set of Tafel curves recorded at 323 K on the porous Ni–Fe–Mo–C–$LaNi_5$ electrode. A curve performed on porous Ni electrode was also included to compare the obtained results. The curves were corrected with respect to the reversible HER potential at the given conditions and for the *jR*-drop. The Tafel curves obtained for porous Ni–Fe–Mo–C–$LaNi_5$

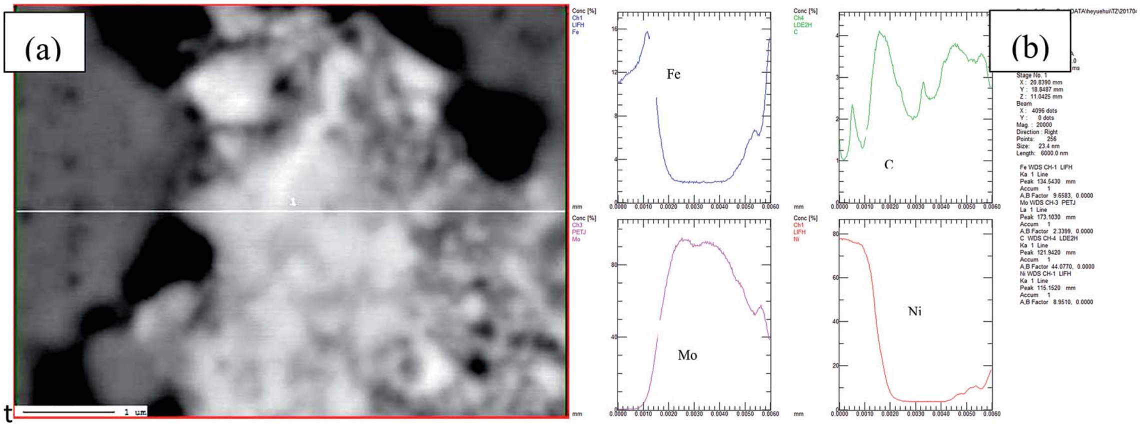

Fig. 5 BSED images (a) and EPMA Line scanning (b) of porous Ni–Fe–Mo–C–$LaNi_5$ electrode, showing the elemental distribution of Ni, Fe, Mo and C.

Table 1 Pore structure parameters of the porous Ni–Fe–Mo–C–$LaNi_5$ cathode material and porous Ni materials

Electrode	Sintering temperature (°C)	Mean pore size (μm)	Porosity (%)
Ni–Fe–Mo–C–$LaNi_5$	820	3.7	35.1
Ni	820	2.1	24

electrocatalysts show a classical Tafe behavior, indicating that the HER on these electrodes is purely kinetically controlled reaction described by the Tafel equation:[43,44]

$$\eta = a + b \log j \tag{1}$$

where η (V) represents the applied overpotential, j (A cm^{-2}) the resulting (measured)current density, b (V $decade^{-1}$) the Tafel

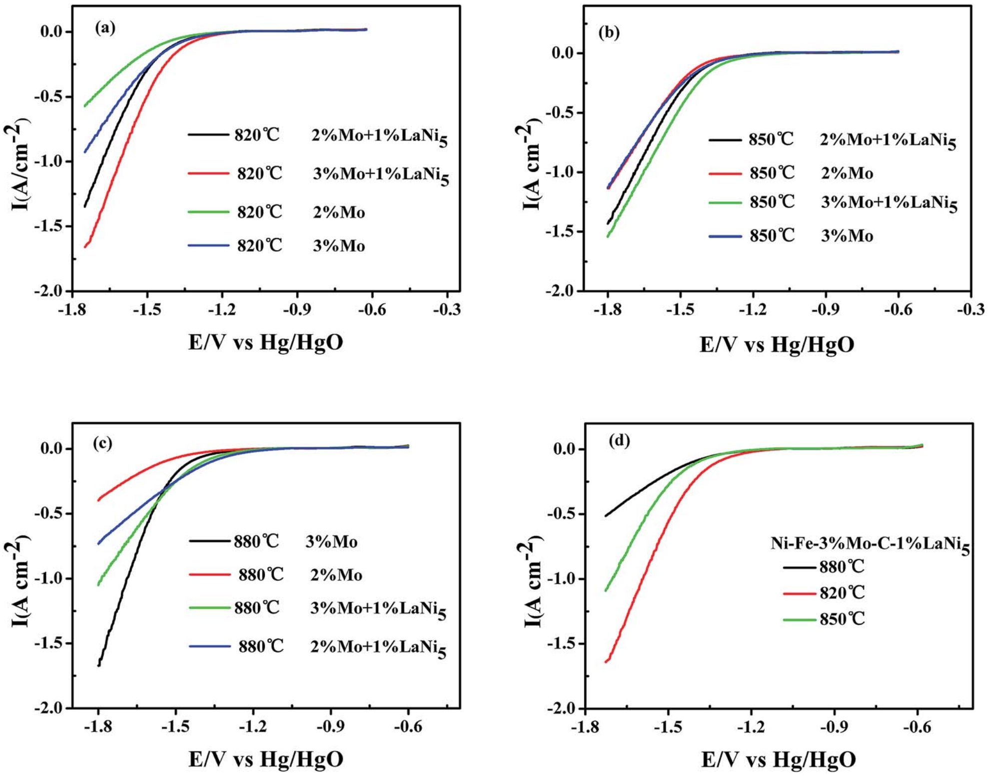

Fig. 6 (a) The cathodic linear sweep for the HER in 6 M KOH on the porous Ni–Fe–Mo–C–$LaNi_5$ cathode materials with different mass ratio at 820 °C; (b) The cathodic linear sweep for the HER in 6 M KOH on the porous Ni–Fe–Mo–C–$LaNi_5$ cathode materials with different mass ratio at 850 °C; (c) The cathodic linear sweep for the HER in 6 M KOH on the porous Ni–Fe–Mo–C–$LaNi_5$ cathode materials with different mass ratio at 880 °C; (d) The cathodic linear sweep for the HER in 6 M KOH on the porous Ni–Fe–Mo–C–$LaNi_5$ cathode materials with different sintering temperature.

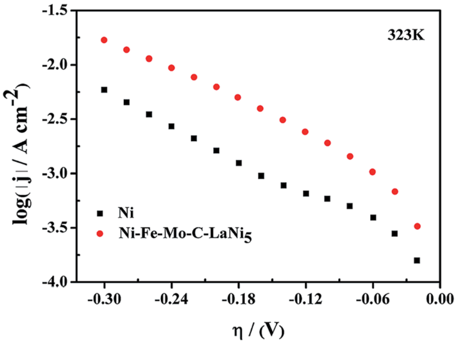

Fig. 7 Linear Tafel polarization curves recorded on smooth Ni, Ni–Fe–Mo–C–LaNi$_5$ electrocatalysts in 6 M KOH solution at 323 K.

slope, and a (V) is the intercept related to the exchange current density j_0 (A cm^{-2}) through equation:

$$a = (2.3RT)/(n\beta F)\log j_0 \tag{2}$$

The other parameter of interest is β, the symmetry factor, which can be calculated from the Tafel slope as

$$b = -(2.3RT)/(n\beta F) \tag{3}$$

and n represents the number of electrons exchanged, F (=96 485 C mol^{-1}) is the Faraday constant, and R (=8.314 J mol^{-1} K^{-1}) is the gas constant. Since curve for porous Ni–Fe–Mo–C–LaNi$_5$ electrocatalyst in Fig. 7 does not show any significant change in the Tafel slope, the same HER reaction mechanism should be valid through the entire overpotential region investigated. The values of the kinetic parameters are reported in Table 2. The mechanism of HER in alkaline solution involves the formation of an adsorbed hydrogen atom intermediate, MH$_{\text{ads}}$ (Volmer reaction, eqn (4)), the electrodic desorption of hydrogen into solution (Heyrovsky reaction, eqn (5)) and/or a chemical desorption by combination of two adatoms (Tafel reaction, eqn (6)):

$$H_2O + M + e^- \rightarrow MH_{ads} + OH^- \tag{4}$$

$$H_2O + MH_{ads} \rightarrow H_2 + M + OH^- \tag{5}$$

$$MH_{ads} + MH_{ads} \rightarrow H_2 + 2M \tag{6}$$

where M is a free site on the metal surface and MH$_{\text{ads}}$ is the metal surface occupied by hydrogen adatoms. When the mechanism is determined from the rate-determining step (RDS) of a multi-step reaction, the Tafel slope plays an important role in estimating the mechanism.[45,46] It has been widely accepted that the value of the charge-transfer coefficient, α, depends on the rds for multi-step reactions.[47–51] Note that for the Volmer step the symmetry factor, β, is equal to the transfer coefficient, α(*i.e.* $\alpha = \beta$) while for the Heyrovsky step the transfer coefficient is equal to $\alpha = \beta + 1$.[52,53] According to the general model for the HER mechanism, when the rds is eqn (4), or eqn (4) coupled with eqn (5), or eqn (4) couple with eqn (6), the value of α is 0.5. Therefore, the Tafel slope becomes 120 mV dec^{-1} at 303 K, and 140 mV dec^{-1} at 353 K. Other possibilities are $\alpha = 1.5$ and $b =$ 40 mV dec^{-1} at 303 K, when eqn (5) is rds; and $\alpha = 2$ and $b =$ 30 mV dec^{-1} at 303 K, when eqn (6) is the rds.[54–56] Here the Tafel slope ranges between 100 mV dec^{-1} and 150 mV dec^{-1} at 303 K and 353 K, respectively, and the $\alpha = \beta$ values are very close to 0.5 for the porous Ni–Fe–Mo–C–LaNi$_5$ electrode (see Table 2). Therefore, following the criteria mentioned above, one can assume that the Volmer step must control the HER on porous Ni–Fe–Mo–C–LaNi$_5$ electrode.

In Table 2 it is also reported the overpotential values at a fixed current density of −100 mA cm^{-2}, η_{100}. This parameter gives an indication on the amount of energy (overpotential) that has to be invested to produce a fixed amount of hydrogen. The current efficiency of the process, determined from the hydrogen volume measured with the aid of the electrochemical cell,[57] is about 99.9%. The porous Ni–Fe–Mo–C–LaNi$_5$ electrode is characterized by higher exchange current density, j_0, and lower hydrogen overpotential, η_{100}, compared to the porous Ni, thereby indicating an improvement of eletrocatalytic activity. Porous Ni–Fe–Mo–C–LaNi$_5$ electrode has the higher exchange current density ($j_0 = 9.9 \times 10^{-4}$ A cm^{-2}, $T = 353$ K) compared to

Table 2 Kinetic parameters of the HER obtained from the polarization curves recorded in 6 M KOH solution at different temperatures

	Temperature (K)					
Catalyst	303	313	323	333	343	353
Ni–Fe–Mo–C–LaNi$_5$						
b (mV dec^{-1})	102.63	109.71	117.48	121.8	134.61	143.67
j_0 (A cm^{-2})	2.82×10^{-4}	4.46×10^{-4}	6.06×10^{-4}	7.07×10^{-4}	8.23×10^{-4}	9.91×10^{-4}
β	0.59	0.57	0.55	0.55	0.51	0.49
η_{100} (100 mv)	262	258	259	260	280	289
Smooth Ni						
b (mV dec^{-1})	94.40	98.23	102.11	128.61	139.18	171.7
j_0 (A cm^{-2})	3.45×10^{-5}	4.61×10^{-5}	5.72×10^{-5}	1.08×10^{-4}	1.20×10^{-4}	3.27×10^{-4}
β	0.64	0.65	0.63	0.52	0.49	0.41
η_{100} (100 mv)	327.8	326.3	332.5	380.0	408.9	428.0

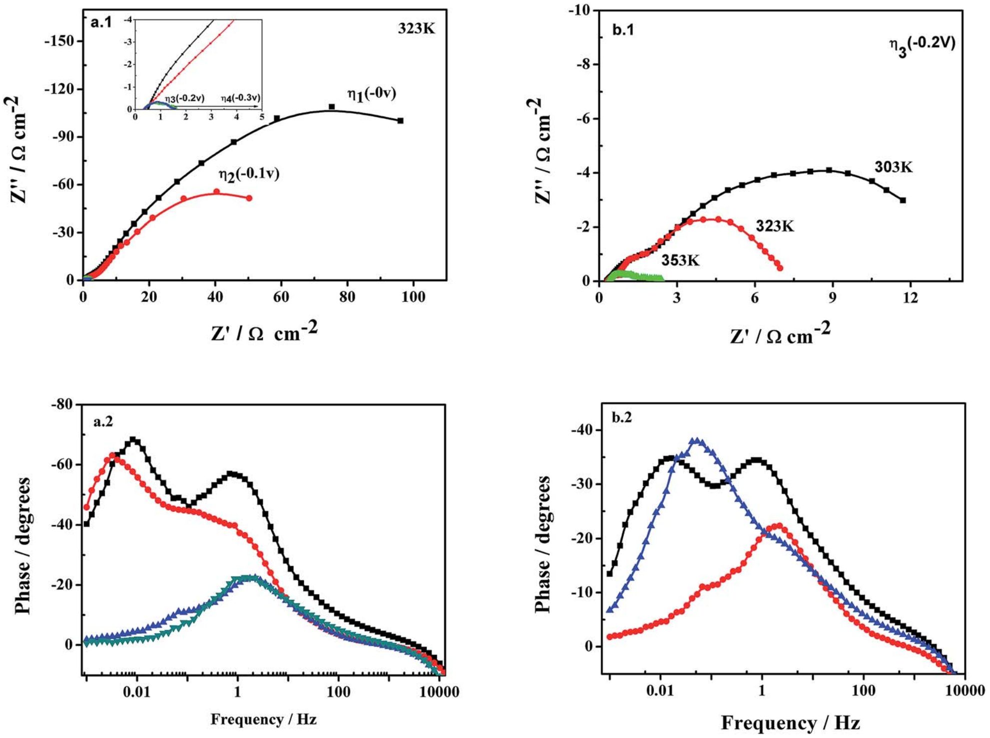

Fig. 8 Impedance data obtained for the porous Ni–Fe–Mo–C/LaNi$_5$ electrode in 6 M KOH solution at: (a) 323 K (effect of overpotential): (a.1) Nyquist representation, (a.2) Bode representation of the phase angle as a function of frequency; and at overpotential (effect of temperature): (b.1) Nyquist representation, (b.2) Bode representation of the phase angle as a function of frequency.

porous Ni–Mo–Fe[58] alloy electrode, porous Ni–Fe–C[59] electrode and porous Ni–Co–LaNi$_5$ (ref. 60) electrode, *etc.* This manifests that porous Ni–Fe–Mo–C–LaNi$_5$ electrode has the better electrocatalytic activity.

However, since the Tafel curves are normalized to the geometric area of the catalysts and not to the real electrochemical area, the results discussed above cannot offer a definite conclusion if the observed electrocatalytic activity is a result of only an increased surface area of the catalysts, or if an improvement in the intrinsic electrocatalytic properties of the catalyst materials is also a contributing factor. Therefore, in order to obtain information on the intrinsic activity of the investigated materials in the HER, the curves presented in Fig. 7 should be normalized to the real electrochemically active surface area. In this work, an EIS technique has been proposed as the most appropriated to determine the real surface area in electrochemical systems. Thus, the following section of the paper will discuss the EIS results obtained in the catalytic materials developed.

3.3. Electrochemical impedance spectroscopy measurements

To ensure a complete characterization of the electrode/electrolyte interface and corresponding processes, EIS measurements were made at different selected overpotentials of the previously obtained polarization curves: η_1, corresponding to the equilibrium potential, 0 mV; η_2, a cathodic overpotential at which it is not manifested the hydrogen evolution; η_3, a overpotential at which the hydrogen production takes place at a very low rate; and η_4, at which hydrogen is vigorously generated. Fig. 8 shows EIS spectra of examples recorded on the Ni–Fe–Mo–C–LaNi$_5$ electrocatalysts. The impedance spectra of the Ni–Fe–Mo–C–LaNi$_5$ electrocatalysts present two clearly differentiated semicircles in the complex plane plot (Fig. 8(a.1)), *i.e.* two maximums in the phase angle Bode representation (Fig. 8(a.2)), being the high frequency semicircle diameter practically constant with the overpotential (see Fig. 8(b.1)). The EIS spectra reveal the presence of two differentiated semicircles (*i.e.* two different time constants), the first one at high frequencies (HF), and the second one, at low frequencies (LF). From Fig. 8 it is clear that the diameter of the LF semicircles diminishes considerably with both the cathodic overpotential and the temperature, whereas the diameter of the HF semicircle remains almost unchanged.

In order to derive a physical picture of the electrode/electrolyte interface and the processes occurring at the electrode surface, a electric equivalent circuit model has been used

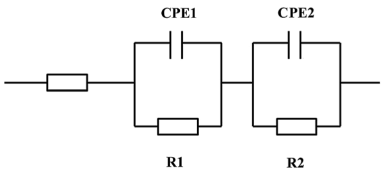

Fig. 9 EEC models used to explain the EIS response of the HER on the Ni–Fe–Mo–C–LaNi$_5$:two-time constant serial model (2 TS).

Table 3 The fitted parameters values of the equivalent for hydrogen evolution reaction on different temperature and different potential

Catalyst	Temperature (K)								
	2 TS EEC								
	303 K			323 K			353 K		
Ni–Fe–Mo–C–LaNi$_5$	0 V	−0.1 V	−0.2 V	0 V	−0.1 V	−0.2 V	0 V	−0.1 V	−0.2 V
χ^2	2.1×10^{-3}	3.5×10^{-3}	6.7×10^{-3}	5.4×10^{-3}	8.2×10^{-3}	6.3×10^{-3}	9.8×10^{-3}	4.9×10^{-3}	6.4×10^{-3}
R_s (Ω cm^2)	0.41	0.41	0.37	0.36	0.33	0.34	0.35	0.34	0.32
R_1 (Ω cm^2)	4.4	5.3	4.5	4.1	3.12	2.19	2.98	2.52	1.78
R_2 (Ω cm^2)	778.1	358.3	13.82	522.7	308	19.78	285.5	41.03	6.17
Q_1 (Ω cm^2)	0.08	0.11	0.16	0.15	0.20	0.23	0.19	0.22	0.26
N_1	0.83	0.82	0.83	0.82	0.82	0.83	0.85	0.84	0.83
C_1 (mF cm^{-2})	39.7	55.7	89.6	79.0	110.1	136.5	117.7	134.3	156.2
Q_2 (Ω cm^2)	0.12	0.19	0.23	0.18	0.24	0.31	0.25	0.33	0.37
N_2	0.85	0.86	0.87	0.88	0.87	0.88	0.89	0.87	0.87
C_2 (mF cm^{-2})	70.5	125.4	159.2	123.9	164.3	228.1	185.0	238.0	269.0
τ_1	0.17	0.30	0.7	0.32	0.34	0.30	0.35	0.34	0.28
τ_2	54.9	44.9	2.2	64.7	50.6	4.5	52.8	9.76	1.66

to fit the EIS response of the catalysis investigated (Fig. 9): a two-time constant serial model. This model, proposed by Chen and Lasia,[61] reflects the response of a HER system characterized by two semicircles, but only the LF semicircle is related to the kinetics of the HER. The time constant associated to this semicircle, τ_2(CPE$_2$ − R_2), changes with overpotential. The HF semicircles is associated to the porosity of the electrode surface,[62–65] and the time constant related to this semicircles, τ_1(CPE$_1$ − R_1), does not significantly change with the cathodic overpotential. According to the discussion presented above, the suitability of a specific electric equivalent circuit (EEC) to model the experimental data can be considered as a criterion to prescribe parameters to the specific processes (*i.e.* charge transfer kinetics, surface porosity or hydrogen adsorption).

Fig. 9 shows that the EEC used properly model the alternating current response of the investigated materials, manifesting an excellent agreement between the experimental (symbols) and CNLS fitting (lines) data. Table 3 reports the EEC parameters values obtained from the experimental impedance data fitting on porous Ni–Fe–Mo–C–LaNi$_5$ electrocatalyst at different temperatures and overpotentials. The equation proposed by Brug *et al.*[66] was employed to average double layer capacitances, C_i, calculations:

$$C_i = [Q_i/(R_s^{-1} + R_i^{-1})^{(1-n)}]^{1/n_i} \qquad (7)$$

With respect to the porous Ni–Fe–Mo–C–LaNi$_5$ electrode, from Table 3 it is clear that HF time constant, τ_1 changes very slightly with both overpotential and temperature, maintaining nearly this parameter in the same order of magnitude, which is usually reported for HF studies on porous electrodes.[67] For the LF semicircle, R_2 decreases with the overpotential and τ_2 decreasing, and that τ_2 varies until two orders of magnitude with overpotential. This behaviour is consistent with the charge transfer phenomenon.

The dependence of C_{dl} as a function of the applied overpotential for the investigated electrodes is presented in Fig. 10. A slow increase of C_{dl} with increasing the applied overpotential is observed in different temperature, indicating that the formation of gaseous hydrogen in the pores does not decrease the real surface area.[68,69] Thence, the increase of C_{dl} values with increasing the overpotential can be correlated with the onset of the faradaic reactions of hydrogen evolution.[70,71] It therefore reflects the electrocatalytic activity of the electrode material, which is in agreement with the polarization curves in Fig. 7. Accordingly, the lowest C_{dl} values were found on the porous Ni–Fe–Mo–C–LaNi$_5$ electrode in 303 K, while the highest values were obtained on the porous Ni–Fe–Mo–C–LaNi$_5$ electrode in 353 K, indicating that this catalyst yields the best catalytic efficiency towards H_2 evolution in high temperature.

Besides the information on the kinetics of the HER, EIS results can be also used to estimate the real surface area of electrocatalytic materials. This is important since by knowing the real electrochemically active area of the catalyst, therefore, it is possible to differentiate the HER intrinsic activity of the materials, by subtracting for the surface area effect. Considering

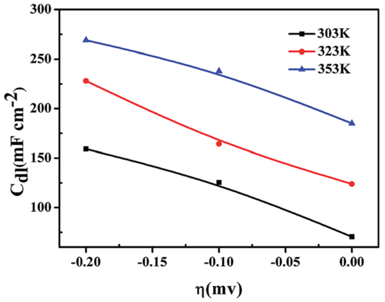

Fig. 10 Trend of the double layer capacitance, C_{dl}, as a function of the HER overpotential for porous Ni–Fe–Mo–C–LaNi$_5$ electrode in 6 M KOH solution at: 303 K, 333 K and 353 K.

Table 4 Double layer capacitance and roughness factor obtained on studied electrodes using the EIS data and CNLS approximation method

Electrode	$C_{dl,ave}$ (mF cm^{-2})	R_f
Ni–Fe–Mo–C–LaNi$_5$		
303 K	118	5900
323 K	172	8600
353 K	231	11 550
Ni	85	4250

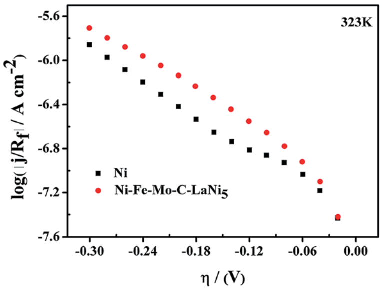

Fig. 11 Linear Tafel polarization curves recorded on Ni–Fe–Mo–C–LaNi$_5$ and Ni electrocatalytic in 6 M KOH solution at 323 K, corrected considering the surface roughness factor, R_f.

a value of 20 μF cm^{-2} for the double layer capacitance, C_{dl}, of a smooth nickel surface area, in term of surface roughness factor (R_f), may be estimated by comparing the C_{dl} related to the HER charge-transfer kinetics of porous/rough and smooth electrodes.[72,73] The plots of the electrode surface roughness factors as function of the HER overpotential are displayed in Table 4.

The R_f values of the latter are in agreement with the small porosity shown in Fig. 2. According to Fig. 11, it can be concluded that porous Ni–Fe–Mo–C–LaNi$_5$ electrode, with an intermediate R_f value, manifests the higher apparent and intrinsic catalytic activities (the low E_a and $|\eta_{100}|$ values) as a result of the synergism between the properties of Ni, Fe, Mo, C and LaNi$_5$ in this composition range and the synthesis conditions.

The increased intrinsic activity of porous Ni–Fe–Mo–C–LaNi$_5$ electrode in comparison to pure Ni is higher. It is well known that the HER electrocatalytic activity of Ni can be improved by the addition of other metals into the alloy. A general conclusion found in the literature is that the intrinsic catalytic activity for the HER is related to the electronic structure of metals, although any explicit and comprehensive explanation has not yet been given.

3.4. Mechanism of hydrogen evolution activity of porous Ni–Fe–Mo–C–LaNi$_5$ electrode

The strength of the H_2O–M and H–M interactions seems to be very important in discussions about surface electrocatalytic effect. In the HER mechanism, the H_2O–M interaction should be strong enough to favor the splitting of the water molecule; conversely, the H–M interaction should not be so strong as to favor hydrogen desorption. In fact, it can be seen from the well-known electrocatalytic "volcano plots" for the HER on the transitional metal, that Fe and Mo exhibit higher electrocatalytic activity because of their intermediate M–H bonding strength. With this assumption, it can be accepted that the Volmer step should be the RDS due to its high-energy requirement in the adsorption and splitting of the water molecule.

As the above discussion, the HER of the porous Ni–Fe–Mo–C–LaNi$_5$ electrode consists on the Volmer reaction and subsequently Tafel reaction. So the porous Ni–Fe–Mo–C–LaNi$_5$ electrode has an intermediate M–H bonding strength and results in the improved electrocatalytic activity for HER. For HER, the Volmer step (the discharge of water molecules) needs paired d-orbital electrons, for instance, Ni d-orbital, to facilitate electron transfer to the water molecule and subsequent cleavage of the O–H bond. For the next step to succeed, semi-empty d-orbitals must be available, for instance, Mo d-orbitals and Fe d-orbitals, to facilitate the M–H desorption. From this point of view, the electrocatalytic effect observed for HER on porous Ni–Fe–Mo–C–LaNi$_5$ surfaces should be enhanced by the appropriate combination of d^8-orbitals of Ni with d^6-orbitals of Fe and d^5 s^1-orbitals of Mo. Volmer step was improved pronouncedly due to the availability of Mo and Fe semi-empty d-orbitals, which facilitates splitting of the water molecule and MH_{ads} formation. LaNi$_5$ enhances the H adsorption on the electrode surface and mainly plays a role of hydrogen storage for hydrogen evolution reaction. Besides, the Ni–Fe–C electrodes with optimum catalytic activity for the HER between carbon content and intrinsic activity are that carbon content plays an important role in intrinsic activity of Ni–Fe–C electrodes discussed by L. J. Song.[74] It was found that Ni–Fe–C cathodes prepared by electrodeposition had high catalytic activity and stability for the HER in sodium hydroxide solution, in which the observed activity was mainly due to the intrinsic activity induced by carbon embedded into Ni–Fe matrix.[37–39] Therefore, this is due to an improved intrinsic activity of the material, which was explained on the basis of the synergism among the catalytic properties of Ni and of Fe, Mo, and induced by C embedded into Ni–Fe matrix and Ni–Fe–Mo matrix. LaNi$_5$ enhances the H adsorption on the electrode surface and mainly plays a role of hydrogen storage for hydrogen evolution reaction.

4. Conclusions

The electrocatalytic efficiency of a porous Ni–Fe–Mo–C–LaNi$_5$ electrode material obtained by reactive synthesis of Ni, Fe, Mo, C and LaNi$_5$ elemental powders in 6 M KOH has been investigated using cathodic polarization and impedance spectroscopy techniques. The Tafel slope of best-performing porous Ni–Fe–Mo–C–LaNi$_5$ alloy is 140 mV dec^{-1}, implying that the RDS for the HER is the proton discharge electrosorption (Volmer reaction). The value for the exchange current density is 9.9×10^{-4} A cm^{-2} at elevated temperature. The roughness factor is 8600, which is obtained for the HER on studied electrodes in 6 M KOH solution at 323 K temperature using the EIS data and CNLS approximation method. Porous Ni–Fe–Mo–C–LaNi$_5$ electrode yields the higher overall electrocatalytic activity in the HER, mainly attributed to the increased surface area. Avoiding the surface roughness factor effect, porous Ni–Fe–Mo–C–$LaNi_5$ electrode manifestes an intrinsic electrocatalytic activity similar to that reported for the pure Ni electrode. This phenomenon can be explained by a proper synergism among the catalytic properties of nickel and of Fe, Mo, and induced by C embedded into Ni–Fe matrix and Ni–Fe–Mo matrix. $LaNi_5$ enhances the H adsorption on the electrode surface and mainly plays a role of hydrogen storage for hydrogen evolution reaction.

Acknowledgements

The authors are grateful for the financial support from the NSF of China (51504213, 51401175, 51271158) and the Project of Hunan province (2015WK3021, 2015JJ3123, 17B250).

References

1 H. B. Gray, *Nat. Chem.*, 2009, **1**, 7.
2 M. Dresselhaus and I. Thomas, *Nature*, 2001, **414**, 332–337.
3 J. A. Turner, *Science*, 2004, **305**, 972–974.
4 K. Zeng and D. Zhang, *Prog. Energy Combust. Sci.*, 2010, **36**, 307–326.
5 M. G. Walter, E. L. Warren, J. R. McKone, S. W. Boettcher, Q. Mi, E. A. Santori and N. S. Lewis, *Chem. Rev.*, 2010, **110**, 6446–6473.
6 Y. Miao, L. Ouyang, S. Zhou, L. Xu, Z. Yang, M. Xiao and R. Ouyang, *Biosens. Bioelectron.*, 2014, **53**, 428–439.
7 P. M. Quaino, M. R. Gennero de Chialvo and A. C. Chialvo, *Electrochim. Acta*, 2007, **52**, 7396–7403.
8 Y. Petrov, J.-P. Schosger, Z. Stoynov and F. de Bruijn, *Int. J. Hydrogen Energy*, 2011, **36**, 12715–12724.
9 U. C. Lacnjevac, B. M. Jovic, V. D. Jovic and N. V. Krstajic, *J. Electroanal. Chem.*, 2012, **31**, 677–680.
10 L. Bai, D. A. Harrington and B. E. Conway, *Electrochim. Acta*, 1987, **32**, 1713–1731.
11 D. E. Hall, *J. Electrochem. Soc.*, 1982, **129**, 310–315.
12 C. Graves, S. D. Ebbesen, M. Mogensen and K. S. Lackner, *Renewable Sustainable Energy Rev.*, 2011, **15**, 1–23.
13 G. Gahleitner, *Int. J. Hydrogen Energy*, 2013, **38**, 2039–2061.
14 B. Conway and B. Tilak, *Electrochim. Acta*, 2002, **47**, 3571–3594.
15 W. Sheng, H. A. Gasteiger and Y. Shao-Horn, *J. Electrochem. Soc.*, 2010, **157**, B1529–B1536.
16 M. Gong, D.-Y. Wang, C.-C. Chen, B.-J. Hwang and H. Dai, *Nano Res.*, 2016, **9**, 28–46.
17 P. Los, A. Rami and A. Lasia, *J. Appl. Electrochem.*, 1993, **23**, 135–140.
18 N. Krstajić, V. Jović, L. Gajić-Krstajić, B. Jović, A. Antozzi and G. Martelli, *Int. J. Hydrogen Energy*, 2008, **33**, 3676–3687.
19 C. Lupi, A. Dell'Era and M. Pasquali, *Int. J. Hydrogen Energy*, 2009, **34**, 2101–2106.
20 S. H. Hong, S. H. Ahn, J. Choi, J. Y. Kim, H. Y. Kim, H.-J. Kim, J. H. Jang, H. Kim and S.-K. Kim, *Appl. Surf. Sci.*, 2015, **349**, 629–635.
21 Y. Zhu, X. Zhang, J. Song, W. Wang, F. Yue and Q. Ma, *Appl. Catal., A*, 2015, **500**, 51–57.
22 I. Paseka, *Electrochim. Acta*, 2001, **47**, 921–931.
23 Q. Han, K. Liu, J. Chen and X. Wei, *Int. J. Hydrogen Energy*, 2003, **28**, 1207–1212.
24 T. V. Vineesh, S. Mubarak, M. G. Hahm, V. Prabu, S. Alwarappan and T. N. Narayanan, *Sci. Rep.*, 2016, **6**, 31202.
25 N. Krstajić, U. Lačnjevac, B. Jović, S. Mora and V. Jović, *Int. J. Hydrogen Energy*, 2011, **36**, 6450–6461.
26 L. Vázquez-Gómez, S. Cattarin, P. Guerriero and M. Musiani, *Electrochim. Acta*, 2007, **52**, 8055–8063.
27 D. A. Dalla Corte, C. Torres, P. dos Santos Correa, E. S. Rieder and C. de Fraga Malfatti, *Int. J. Hydrogen Energy*, 2012, **37**, 3025–3032.
28 Z. Chen, Z. Ma, J. Song, L. Wang and G. Shao, *RSC Adv.*, 2016, **6**, 60806–60814.
29 Z. Zheng, N. Li, C.-Q. Wang, D.-Y. Li, F.-Y. Meng and Y.-M. Zhu, *J. Power Sources*, 2013, **222**, 88–91.
30 Z. Chen, Z. Ma, J. Song, L. Wang and G. Shao, *J. Power Sources*, 2016, **324**, 86–96.
31 D. Ansovini, C. J. J. Lee, C. S. Chua, *et al.*, *J. Mater. Chem. A*, 2016, **4**, 25.
32 L. Yu, T. Lei, B. Nan, *et al.*, *RSC Adv.*, 2015, **5**(100), 82078–82086.
33 I. Arul Raj, *Int. J. Hydrogen Energy*, 1992, **17**, 413.
34 I. Arul Raj, *Appl. Surf. Sci.*, 1992, **59**, 245.
35 I. Arul Raj, *J. Appl. Electrochem.*, 1992, **22**, 471.
36 W. Hu, Y. Zhang, D. Song, Z. Zhou and Y. Wang, *Mater. Chem. Phys.*, 1995, **41**, 141.
37 S. Meguro, T. Sasaki, H. Katagiri, H. Habazaki, A. Kawashimac, T. Sakaki, *et al.*, *J. Electrochem. Soc.*, 2000, **147**, 3–9.
38 K. Hashimoto, M. Yamasaki, S. Meguro, H. Habazaki, A. Kawashima, T. Sasaki, *et al.*, *Corros. Sci.*, 2002, **44**, 71–86.
39 R. K. Shervedani and A. R. Madram, *Electrochim. Acta*, 2007, **53**, 26–33.
40 K. Machida and M. Enyo, *Electrochim. Acta*, 1984, **29**, 1723.
41 Y. Xiao, Y. Liu, Z. Tang, L. Wu, Y. Zeng, Y. Xu, *et al.*, *RSC Adv.*, 2016, **6**, 51096–51105.
42 Y. Jiang, Y. H. He, N. P. Xu, J. Zou, B. Y. Huang and C. T. Liu, *Intermetallics*, 2008, **16**, 27–32.
43 P. Los, A. Rami and A. Lasia, *J. Appl. Electrochem.*, 1993, **23**, 35–40.
44 L. L. Chen and A. Lasia, *J. Electrochem. Soc.*, 1991, **138**, 1–8.
45 L. L. Chen and A. Lasia, *J. Electrochem. Soc.*, 1992, **139**, 58–64.
46 J. O. Bockris and A. K. N. Reddy, *Modern electrochem*, Kluwer/Plenum Press, New York, 2nd edn, 2000.
47 L. L. Chen and A. Lasia, *J. Electrochem. Soc.*, 1992, **139**, 4–9.
48 P. Los, A. Rami and A. Lasia, *J. Appl. Electrochem.*, 1993, **23**, 35–40.
49 L. L. Chen and A. Lasia, *J. Electrochem. Soc.*, 1991, **138**, 1–8.
50 A. Rami and A. Lasia, *J. Appl. Electrochem.*, 1992, **22**, 76–82.
51 A. C. D. Angelo and A. Lasia, *J. Electrochem. Soc.*, 1995, **142**, 3–9.
52 Southampton Electrochemistry Group, *Instrumental methods in electrochemistry*, Wiley, New York, 1985.

53 J. G. Highfield, E. Claude and K. Oguro, *Electrochim. Acta*, 1999, **44**, 5–14.
54 M. P. M. Kaninski, V. M. Nikolic, T. N. Potkonjak, B. R. Simonovic and N. I. Potkonjak, *Appl. Catal., A*, 2007, **321**, 3–9.
55 A. Metikos-Hukovic, Z. Grubac, N. Radic and A. Tonejc, *J. Mol. Catal. A: Chem.*, 2006, **249**, 72–80.
56 F. Rosalbino, S. Delsante, G. Borzone and E. Angelini, *Int. J. Hydrogen Energy*, 2008, **33**, 696–703.
57 J. García-Antón, E. Blasco-Tamarit, D. M. García-García, V. Guiñón-Pina, R. Leiva-García and V. Pérez-Herranz, ESP. Pat., 03389, 2008.
58 M. Wang, Hunan university (HNU), 2014.
59 R. K. Shervedani and A. R. Madram, *Electrochim. Acta*, 2007, **53**, 426–433.
60 G. Wu, N. Li, C. S. Dai, *et al.*, *Mater. Chem. Phys.*, 2004, **83**, 307–314.
61 L. L. Chen and A. Lasia, *J. Electrochem. Soc.*, 1991, **138**, 1–8.
62 B. Losiewicz, A. Budniok, E. Rowinski and A. Lasia, *Int. J. Hydrogen Energy*, 2004, **29**, 45–57.
63 L. Birry and A. Lasia, *J. Appl. Electrochem.*, 2004, **34**, 35–49.
64 B. Borresen, G. Hagen and R. Tunold, *Electrochim. Acta*, 1997, **42**, 1–9.
65 J. Kubisztal, A. Budniok and A. Lasia, *Int. J. Hydrogen Energy*, 2007, **32**, 1211–1218.
66 G. J. Brug, A. L. G. Vandeneeden, M. Sluytersrehbach and J. H. Sluyters, *J. Electroanal. Chem.*, 1984, **176**, 72–95.
67 L. Vazquez-Gomez, S. Cattarin, P. Guerriero and M. Musiani, *J. Electroanal. Chem.*, 2009, **634**, 2–8.
68 J. R. MacDonald, J. Schooman and A. P. Lehner, *J. Electroanal. Chem.*, 1982, **131**, 77.
69 J. Divisek, *J. Electroanal. Chem.*, 1986, **214**, 615.
70 L. Chen and A. Lasia, *J. Electrochem. Soc.*, 1992, **139**, 3458.
71 H. Alemu and K. Jüttner, *Electrochim. Acta*, 1988, **33**, 1101.
72 A. Kellenberger, N. Vaszilcsin, W. Brandl and N. Duteanu, *Int. J. Hydrogen Energy*, 2007, **32**, 58–65.
73 J. Kubisztal, A. Budniok and A. Lasia, *Int. J. Hydrogen Energy*, 2007, **32**, 1–8.
74 L. J. Song and H. M. Meng, *Int. J. Hydrogen Energy*, 2010, **35**, 10060–10066.